Chinese Journal of Aeronautics, (2014),27(5): 1128–1136

Chinese Society of Aeronautics and Astronautics
& Beihang University

Chinese Journal of Aeronautics

cja@buaa.edu.cn
www.sciencedirect.com

Design and numerical investigation of swirl recovery vanes for the Fokker 29 propeller

Wang Yangang [a,*], Li Qingxi [a], G. Eitelberg [b,c], L.L.M. Veldhuis [b], M. Kotsonis [b]

[a] School of Power and Energy, Northwestern Polytechnical University, Xi'an 710072, China
[b] School of Aerospace Engineer, Delft University of Technology, Delft 2629 HS, The Netherlands
[c] German-Dutch Wind Tunnels, Marknesse 8316PR, The Netherlands

Received 1 November 2013; revised 12 December 2013; accepted 19 February 2014
Available online 18 March 2014

KEYWORDS

Multiple circular airfoil;
Propellers;
Propulsion efficiency;
Swirl recovery vane;
Turboprop engine

Abstract Swirl recovery vanes (SRVs) are a set of stationary vanes located downstream from a propeller, which may recover some of the residual swirl from the propeller, hoping for an improvement in both thrust and efficiency. The SRV concept design for a scaled version representing the Fokker 29 propeller is performed in this paper, which may give rise to a promotion in propulsive performance of this traditional propeller. Firstly the numerical strategy is validated from two aspects of global quantities and the local flow field of the propeller compared with experimental data, and then the exit flow together with the development of propeller wake is analyzed in detail. Three kinds of SRV are designed with multiple circular airfoils. The numerical results show that the swirl behind the propeller is recovered significantly with Model V3, which is characterized by the highest solidity along spanwise, for various working conditions, and the combination of rotor and vane produced 5.76% extra thrust at the design point. However, a lower efficiency is observed asking for a better vane design and the choice of a working point. The vane position is studied which shows that there is an optimum range for higher thrust and efficiency.

1. Introduction

Arising from the rapid developments of unmanned air vehicles and ultralight vehicles, the emerging market of general aviation, and the emphasis on environmental issues, much more attention is being focused on propeller propulsion devices from researchers, enterprises, and governments, so as to have multiple choices of economical and environmentally friendly propulsion systems.[1–3]

The concept of high-speed and high-efficiency propeller propulsion has come to the fore after the energy crisis started in the mid-1970s, and it showed an incomparable performance advantage over an equivalent technology – turbofans in a systematic investigation and study.[4] At a cruising speed of 240 m/s the installed efficiency of newly developed advanced turboprop would be approximately 80% compared to about 65% for turbofan systems, additionally with fuel savings ranging from

* Corresponding author. Tel.: +86 29 88495911.
E-mail addresses: wyg704@nwpu.edu.cn (Y. Wang), lqxymds@mail.nwpu.edu.cn (Q. Li).

Peer review under responsibility of Editorial Committee of CJA.

ELSEVIER Production and hosting by Elsevier

http://dx.doi.org/10.1016/j.cja.2014.03.009

15% to 30%.[5] A series of enabling technologies made it effective in these functions: thinner and wider swept blades, increased number of blades, and area-ruled spinner nacelle.[6–8] These new technologies not only made it possible for the section Mach number to be lower than the drag divergence Mach number, which led to a sharp decrease of compressibility losses, but also provided a new choice for noise reduction which was an intractable challenge for designers.[9] Swept blades were employed to reduce propeller source noise and a double-wall fuselage construction was developed to improve fuselage wall noise attenuation.[10]

As depicted in Ref.[5], the swirl induced by a propeller accounted for 7%–11% of total loss at the cruise condition of 240 m/s and 10.668 km altitude. The concept of counter-rotation propeller (CRP) was then proposed and proved to be more efficient due to the ability of the second rotating stage to recover and make use of the swirl present in the propeller slipstream.[11] The net efficiency of the National Aeronautics and Space Administration (NASA) counter-rotation propeller verification model CRP-X1 reached a level of approximately 85% at cruising velocity ranging from 210 m/s to 240 m/s, and maintained at a high level over a wide range of power loadings.[12] A technology-demonstrating airplane on a CRP was produced by Lockheed-Georgia, for which an 8% fuel saving and a 2.5% direct operating cost reduction were estimated.[13] Moreover, some control and structural benefits were observed on CRP airplanes including a considerable cancellation of torque and gyroscopic loads, enhanced aircraft flutter stability, and improved aerodynamic integration due to slipstream swirl removal.

However, it is also clear that some inherent flaws do exist in CRP systems although the advantage of high efficiency impresses and attracts every of us, some of which are increases both in the weight of the propulsion system and the interaction noise of the counter-rotating stage, as well as additional complication in the structural form. Whereas, if the second rotating stage is replaced by a fixed row of vanes, it would be possible to maintain the ability of recovering swirl without the complexity of a CRP which comes to a compromise between aerodynamic performance and structural complication level. This was proposed and named swirl recovery vane (SRV) by NASA on the purpose of obtaining higher efficiency in the high-speed propeller program.[14] The experimental data demonstrated that a 2% efficiency increment was measured at a 240 m/s cruising speed and 4.5% at 180 m/s.[15] The use of SRVs shifted the peak of propeller efficiency to a higher operating speed without any extra remarkable noise. As of now, there is still a lack of detailed research on SRVs.

In this paper, a set of SRVs was designed for the Fokker 29 propeller, and the design was conducted at a takeoff condition considering experimental resources. Firstly the numerical strategy was validated, which was followed by the analysis of the interaction between the rotor and the vanes. Three kinds of SRV were obtained to explore the influence of the chord length profile, and the axial positions of vanes were also studied here.

2. Validation of numerical methods

2.1. Propeller model

The scaled model of a 4-bladed propeller was employed here with a radius of $R = 0.1524$ m, the incidence angle at $3R/4$ set to 40°, and the hub radius $r_{hub} = 0.042$ m (see Fig. 1). The original was used as the tractor propeller on Fokker 29 airplanes.

2.2. Experiments at Delft University of Technology (TU Delft)

As a part of the EU-funded project ESPOSA (Efficient Systems and Propulsion for Small Aircraft), wind tunnel experiments were conducted in the Low-Speed Tunnel (LST) of German-Dutch Wind Tunnels (DNW) by TU Delft researchers.[16]

The tests were performed in the 3 m × 2.25 m test section of the DNW-LST facility. The test setup consists of an air motor that powers the 4-bladed propeller. The cylindrical nacelle that houses the air motor is supported by a streamlined strut that carries the high-pressure air supply piping.

The 4-bladed Fokker F29 experimental propeller is directly coupled to a 6-component rotating shaft balance (RSB) which measures the isolated thrust, torque, normal force, and moment produced by the propeller. To correct for the changing pressure that acts on the back side of the spinner, pressure data were recorded on the back plate of the RSB. All relevant wind tunnel wall corrections have been applied. In addition to the RSB measurements, 5-hole probe traverses behind the propeller were performed in order to get detailed insight in the flow field produced by the propeller.

2.3. Numerical strategy

The presented numerical predictions were carried out with the NUMECA commercial solver. The computation domain was thus defined, as illustrated in Fig. 2, by a segment of a cylinder, covering only one blade. This was finally decided through a domain-independence study varying the external boundaries in front of, behind, and out of the propeller until reaching sufficient accuracy in the propeller propulsive performance. The spinner was described by an ellipse to comply with the experimental situation as much as possible, the center of which was located at the origin. The same elliptical shape was used as compensation 0.35 m downstream from the spinner center which is far enough from the propeller. The inlet/outlet was 0.65 m upstream/downstream from the origin, while the outer boundary was set as far as $2R$.

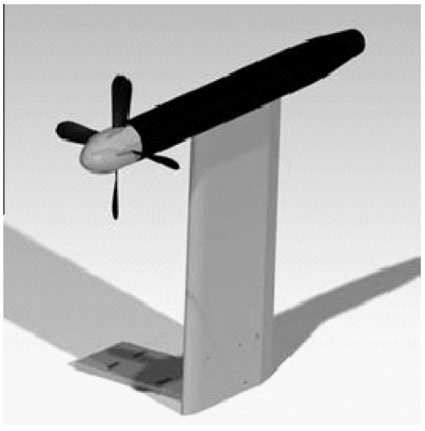

Fig. 1 Test setup of an isolated propeller.

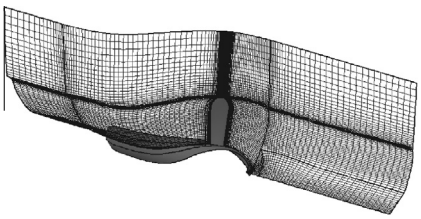

Fig. 2 3D sketch of the computation domain.

2.4. Grid generation

Three hexa-structured meshes with different resolution levels were generated (see Table 1). The main difference lay in the number of grid layers. The ratio of grid layers of the blade area to the outer area was set to 3:2 to reach a compromise between the accuracy of global performance and the capture of the tip vortex. The distance of the first node from the solid surfaces was set to 10^{-5} m, and consequently the value of y^+ was kept below 10.

2.5. Solution of the flow field

The numerical simulation was performed under the condition of $J = 1.00$, where J is the advance ratio. The flow field was set following the experimental setup, i.e., the free stream velocity $V_\infty = 30$ m/s, the rotation speed 5915 r/min corresponding to $J = 1.00$. Viscous forces and torque of hub were not taken into account in the final results. The steady three-dimensional Navier–Stokes equations coupled with the Spalart–Allmaras turbulence model were solved with a central difference scheme for spatial discretization.

2.6. Results and discussion

Global quantities, represented by the relative errors ΔC_T and ΔC_Q, were compared between numerical results and experimental data (see Fig. 3), as well as a selection of local field values computed in a plane located downstream from the propeller. C_T and C_Q together with ΔC_T and ΔC_Q were defined as follows:

$$C_T = \frac{T}{\rho n_s^2 D^4} \tag{1}$$

$$C_Q = \frac{Q}{\rho n_s^2 D^5} \tag{2}$$

$$\Delta C_T = \frac{C_{T_{CFD}} - C_{T_{EXP}}}{C_{T_{EXP}}} \times 100\% \tag{3}$$

$$\Delta C_Q = \frac{C_{Q_{CFD}} - C_{Q_{EXP}}}{C_{Q_{EXP}}} \times 100\% \tag{4}$$

where T is the thrust, Q the torque, n_s the rotation speed, D the diameter of the propeller, and ρ the density of the fluid.

Table 1 Number of grids for different resolution types.

Grid	Number of nodes (10^6)
Coarse	1.13
Mid	1.51
Fine	2.02

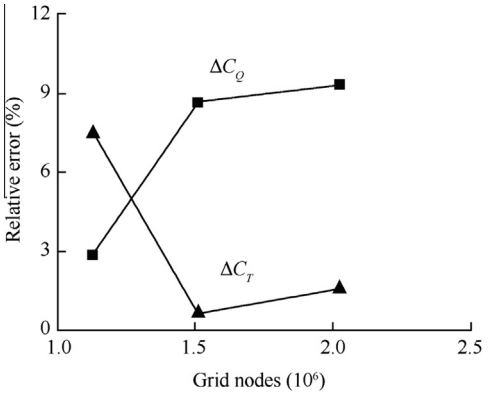

Fig. 3 Relative errors of numerical results compared with experimental data.

As shown in Fig. 3, ΔC_T decreases significantly when the number of grid nodes changes from 1.1×10^6 nodes to 1.5×10^6 nodes, while meshes with mid and fine resolutions show little difference, which is indicative of the preference of the mid grid. The same conclusion can be made by the analysis of ΔC_Q.

As far as the local flow field, the circumferentially averaged outflow angle β_2 was evaluated in the plane $z/R = 0.26$, where z is the axial distance from the trailing edge of the propeller and R is the propeller radius. A small sketch in the top right corner of Fig. 4 shows how β_2 is defined in reference with the rotation direction ω. In general, the predicted values are larger than those from experiments, at a level of 1.5°. In the blade area, three types of grids show little difference; while in the outer area, the coarse grid has a much greater fluctuation than both the experimental data and the mid or fine grid, again giving more confidence for the use of the mid grid.

In general terms, the predictions carried out on the mesh with the mid resolution were more preferable considering accuracy and computational time.

3. Numerical simulation on isolated propeller

3.1. Total performance

It should be mentioned that the number of blades was changed from 4 to 8. The thrust coefficient, torque coefficient, and

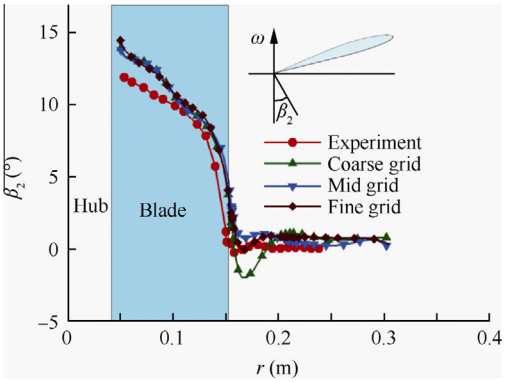

Fig. 4 Comparison of outflow angle between predicted values and experiment data.

efficiency of the propeller were plotted over a wide range of advance ratios in Fig. 5, wherein efficiency was defined as:

$$\eta = \frac{JC_T}{2\pi C_Q} \tag{5}$$

As shown in Fig. 5, C_T and C_Q decrease linearly with the increment of advance ratio, while the variation of efficiency is a curve peaking at 68.2%. The reduction from the peak with increasing advance ratio is due to lower blade sectional lift-to-drag ratios (from increasing incidence angles). The fall-off with decreasing advance ratio results from increased compressibility losses associated with higher tip rotational speeds and/or again lower blade sectional lift-to-drag ratios (from decreasing local incidence angles).

3.2. Flow structure analysis of slipstream zone

It is quite necessary to get a deep insight into the flow structure and wake development of the propeller slipstream zone to provide a reference for the design of SRVs. Here the flow field of the propeller operating at $J = 1.00$ was collected as an example for this study and also the design point of SRVs.

Fig. 6 demonstrates the absolute velocity streamlines in the $rO\theta$ plane at the position of $z/R = 0.15$ downstream from the blades with the axial velocity (normalized by the free stream velocity) highlighted in the background, blades rotating in the clockwise direction. Only one passage was calculated which means that the left and right boundaries were set to periodic conditions. The influence of the tip vortex and the radial distribution of the radial velocity as well as the low-speed region at radial stations near the hub can be easily recognized in this figure.

Contraction appears in the slipstream due to the increment of the axial velocity, while the tip vortex does not change much in the radial position. The dominant feature of this flow is the vortical structure near the tip of the blade. The center of the vortex responds to the minimum axial velocity region. Large gradient in the axial velocity can be seen radiating from the heart of the vortex, for the reason that the vortex axis is inclined to the plane, and thus a portion of the rotational velocity associated with the vortex is resolved in the axial direction.

The changes in circulation at different radial positions result in the shed vortex sheet, whose strength is proportional

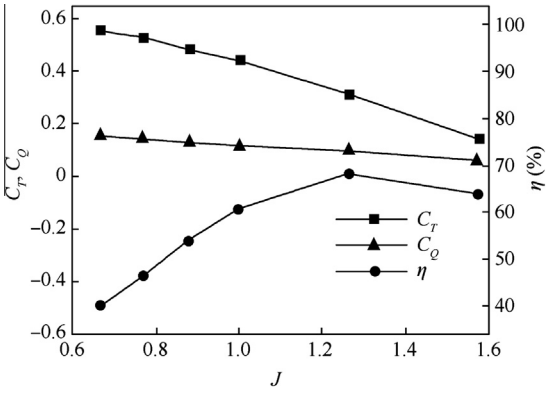

Fig. 5 Propulsive performance of the isolated propeller.

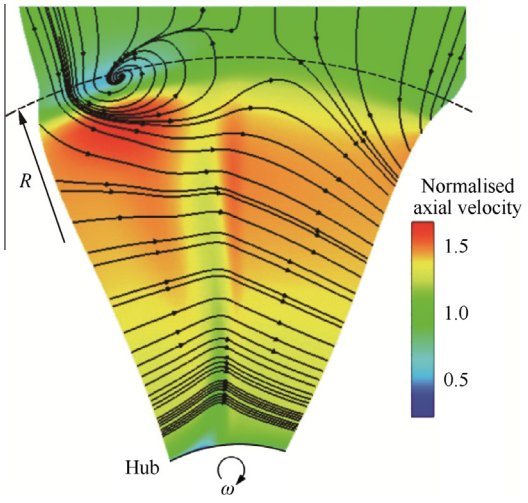

Fig. 6 Velocity profile at $z/R = 0.15$.

to $d\Gamma/dr$, where Γ is the sectional circulation. The loading under this condition was expected to be low at the hub, increasing up to $r/R = 0.6$, nearly constant until $r/R = 0.9$, and rapidly falling to zero at the tip. This rapid falloff in blade loading near the tip is the cause of the tip vortex. At the inboard stations, there is a definite jump in radial velocity characterized by a protruding shape which is indicative of increasing blade loading. Between $r/R = 0.6$ and $r/R = 0.9$, there is little change in radial velocity because of nearly constant blade loading. At the tip of the blade, the radial velocity jump is reversed, forming the tip vortex. The same conclusion has been made in Ref.[17] that examination of the radial velocity component is a good diagnosis for verifying blade loading predictions.

In the region adjacent to the hub, the flow field is mainly affected by viscous forces, which experiences almost no acceleration. This part of low kinetic energy fluid mixes with that from the shed boundary layer of blades, composing a main part of loss.

To have a better understanding of the development of propeller wake flow, the axial distributions of the axial velocity V_z were illustrated in Fig. 7. The results were collected at $r/R = 0.57$, which is in the core-flow region behind the propeller and away from the tip or hub effects. The initial plane is located at $z/R = 0.03$ just behind the propeller.

The propeller wake flow decays rapidly along the axial position, which can be seen from the soon "filled" minimum velocity acting as a sharp valley in Fig. 7(a) as well as the width in tangential extent. To know the rate of this decay quantitatively, the maximum velocity deficit δ_{V_z} and the width of blade wake δ_θ are shown in Fig. 7(b), which are defined as:

$$\delta_{V_z} = \frac{V_{z_{\text{avg}}} - V_{z_{\min}}}{V_{z_{\text{avg}}}} \tag{6}$$

$$\delta_\theta = \frac{\theta_{\text{wake}}}{\theta_{\text{blade}}} \tag{7}$$

where $V_{z_{\text{avg}}}$ is the mean axial velocity, $V_{z_{\min}}$ the minimum axial velocity, θ_{wake} the tangential extent of blade wake, and θ_{blade} is one blade spacing in circumference which is 45° for an 8-bladed propeller. As shown above, δ_{V_z} decays rapidly before $z/R = 0.4$ as a result of the strong shear stress existing in large

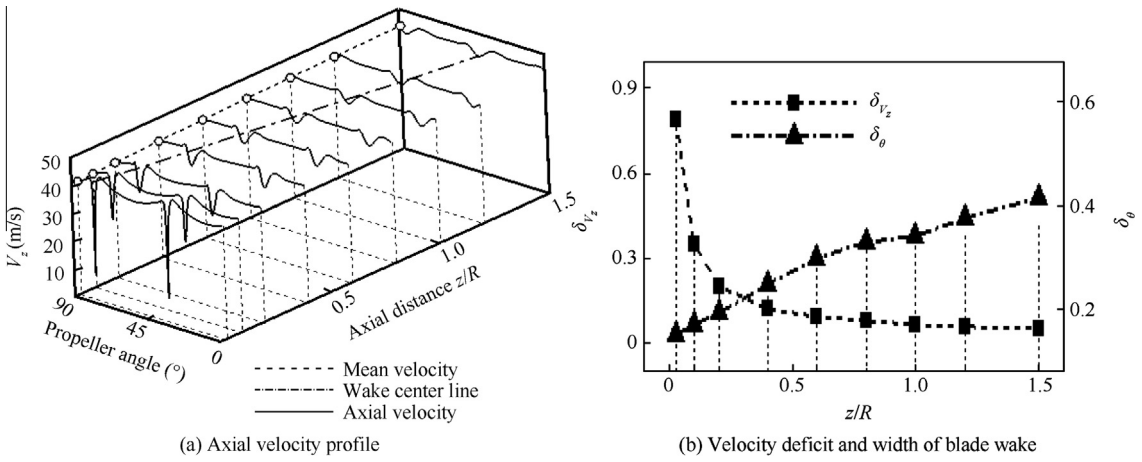

(a) Axial velocity profile (b) Velocity deficit and width of blade wake

Fig. 7 Wake decay behind isolated propeller, $r/R = 0.57$ and $J = 1.00$.

velocity gradient, which has fallen to 15% of that of the initial plane at $z/R = 0.4$ reaching a level of 6% ultimately at $z/R = 1.5$. The velocity of the main flow region decreases at the junction with the blade wake region resulting from momentum exchange. The inflow condition may change dramatically when an SRV is too close to the propeller blade, which not only might cause great loss in thrust and efficiency, the exciting forces may also lead to an unwilling increase in blade thickness and at last total weight.

The mean axial velocity is plotted as a dashed line in Fig. 7(a). The mixing loss gives it a downward trend while the thrust from the propeller accelerates the flow, so in the end, the mean velocity has increased a little. The center of the blade wake region, i.e., the position of the minimum velocity, is shown as a dash dot line in Fig. 7(a). This line is at an angle to the axis by the blade dragging the fluid in the tangential direction. The main task of SRVs is just to minimize or eliminate the tangential motion of the fluid behind the propeller.

4. Design and aerodynamic analysis of SRVs

4.1. Design of SRVs

The SRVs were designed under the condition of $J = 1.00$ and $V_\infty = 30$ m/s aiming at a uniform circumferentially-averaged outflow angle. The distance between the stacking point of rotor and vane was set to $2c_0$ where c_0 is the chord length of the rotor root. The outflow angle of the isolated propeller at this position was collected as the inflow condition for SRVs, and the incidence angle was chosen at $-2.5°$ so that the geometry inflow angles of SRVs were obtained. The elementary blades were designed on seven elements (see Fig. 8).

Multiple circular arc airfoils were adopted. The changing rates of the angle between two arcs composing the mean camber line, the suction line, and the pressure line were set to a constant respectively. The airfoils designed on sections were stacked forming the blade surface.

Three types of SRV were designed with different chord length profiles, of which the chord length c refers to c_0. The relationship between the chord lengths of SRVs and the propeller for three models was exhibited in Fig. 9, denoted as Models V1, V2, and V3. SRVs have a straight shape for Model V1 and a divergent shape for Models V2 and V3, which means that the chord length along the spanwise direction increases gradually, to allow a larger consistent value in outboard stations. It has a maximum thickness of 3 mm, of which the position conforms to that of the turning point, both at the midpoint of the mean camber line. The radius of SRVs ($R_{\text{Vane}} = 0.14$ m) is a bit smaller than that of the propeller ($R = 0.1524$ m) to get away from the tip vortex. The geometric outflow angle of SRVs was adjusted during the design procedure to get a uniform value of outflow angle behind SRVs.

The grids have a total number of 2.56×10^6 nodes, of which 1.06×10^6 are from the propeller stage, 1.11×10^6 from the SRV stage, and 0.39×10^6 from inlet and outlet junctions. A mixing plane approach was applied at the rotor/stator interfaces, which means that the rotor–stator interaction was done by exchanging circumferentially-averaged flow quantities.

4.2. Total performance analysis

The thrust coefficient of SRVs was defined referring operating parameters of the propeller, while total performance quantities were also calculated to allow a comparison between the isolated propeller and the combination of rotor and vane:

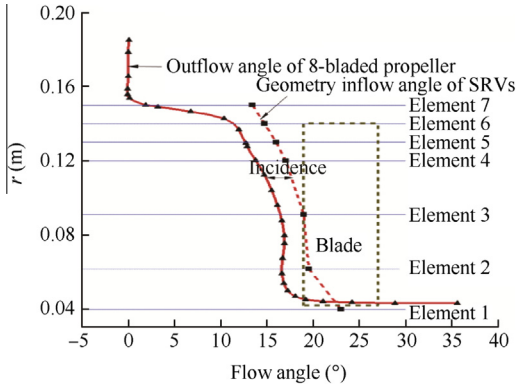

Fig. 8 Reference inflow condition for design of SRVs.

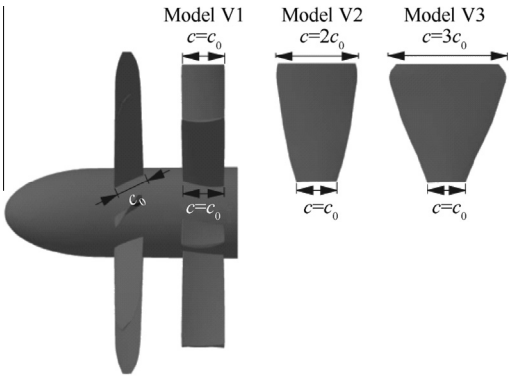

Fig. 9 3D sketches of Models V1, V2, and V3.

$$C_{T_{\text{Vane}}} = \frac{T_{\text{Vane}}}{\rho n_s^2 D_{\text{Vane}}^4} \tag{8}$$

$$C_{T_{\text{Total}}} = \frac{T_{\text{Total}}}{\rho n_s^2 D_{\text{Rotor}}^4} \tag{9}$$

$$\eta_{\text{Total}} = \frac{C_{T_{\text{Total}}} J}{C_{Q_{\text{Rotor}}} \cdot 2\pi} \tag{10}$$

where T_{Vane} is the thrust of SRVs and D_{Vane} is the SRV diameter. T_{Total} is obtained by algebraic summation of the thrust of propeller and vane, but pressure and shear forces of the hub were not taken into account.

The comparison was illustrated in Fig. 10. $C_{T_{\text{Total}}}$ has increased with all three kinds of SRVs but shows little difference (see Fig. 10(a)). The possible reason may lie in that an SRV has a block effect on the flow behind the propeller, thus

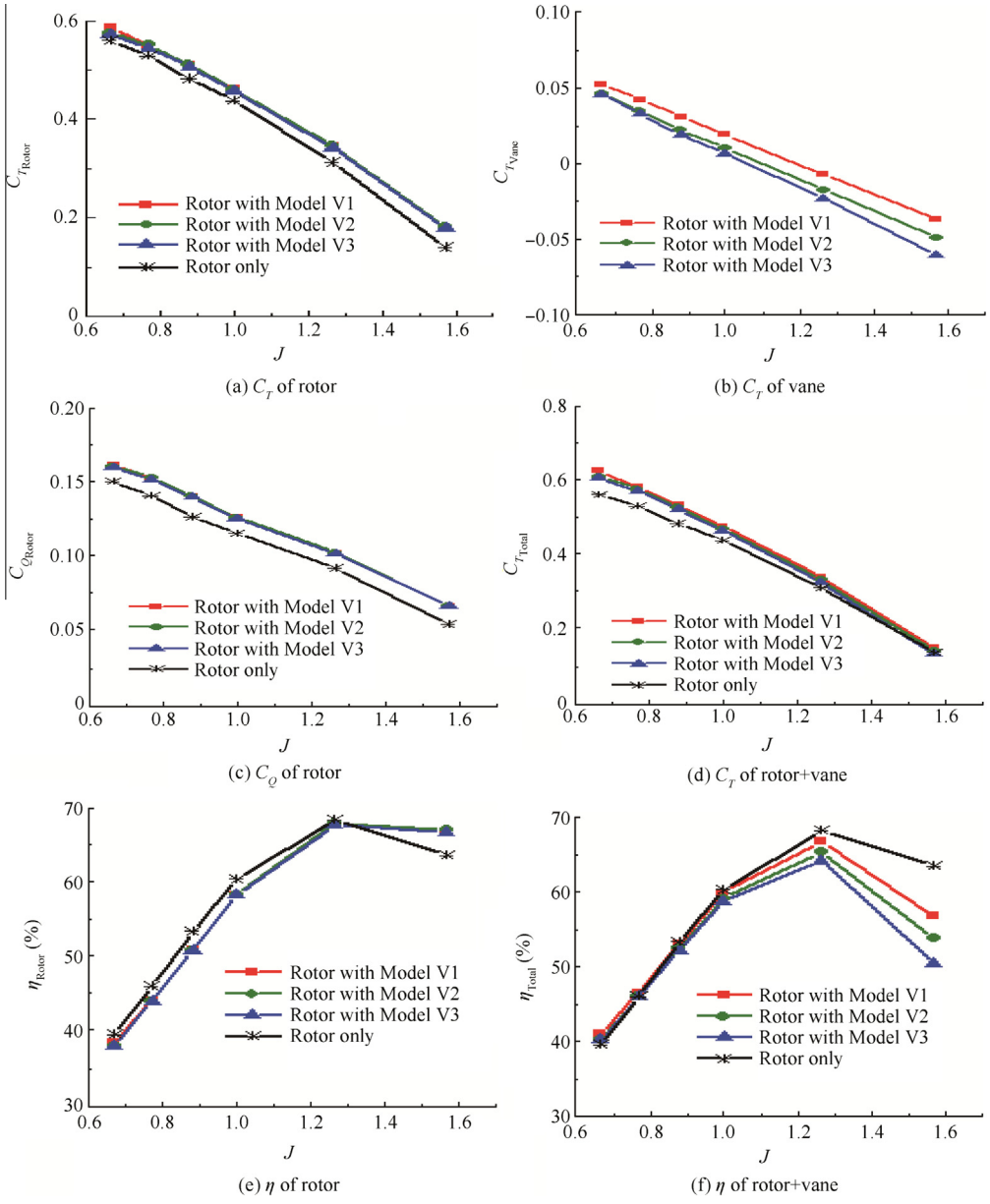

Fig. 10 Total performance of the propeller with different SRV models.

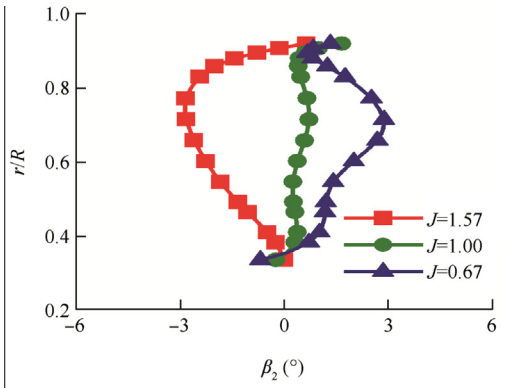

(a) Outflow angle with Model V3

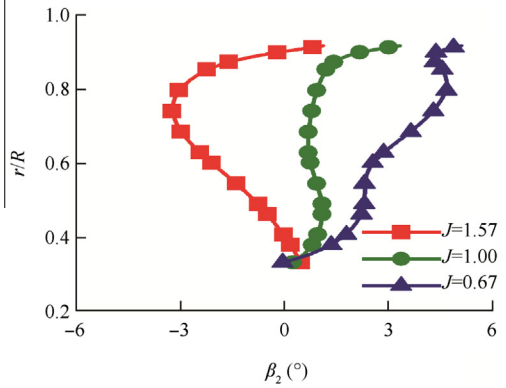

(b) Outflow angle with Model V2

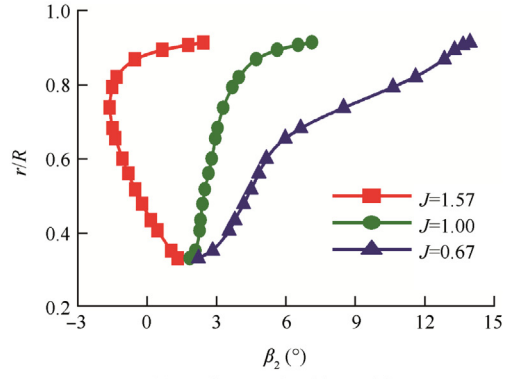

(c) Outflow angle with Model V1

Fig. 11 Outflow angle profiles for different models.

limiting the flow capacity, and the incidence angle for propeller blade sections increases as a result, so do the blade loads.

The vanes generate thrust or drag under different operating conditions: drag appears when the propeller rotates at low speeds and SRVs at large negative incidences, while on the opposite, thrust is generated. Model V1 tends to have the largest thrust coefficient among the three models. Compared with the rotor thrust coefficient $C_{T_{\text{Rotor}}}$, $C_{T_{\text{Total}}}$ exhibits a larger difference at lower advance ratios due to the addition of a positive thrust of SRVs. This difference has compressed gradually with the reduction of vane thrust and the increment of negative values appearing at large advance ratios.

The power absorbed by the propeller with SRVs surpasses that by the isolated propeller although the thrust mounts as well, which is responsible for the reductions of η_{Rotor} and η_{Total}. The total efficiency diminishes much more distinctly at high advance ratios because of the negative thrust of SRVs.

In Fig. 11, the circumferentially-averaged outflow angle at a distance of $z/c_0 = 0.5$ behind SRVs was plotted versus radial positions under three typical conditions ($J = 1.57$, $J = 1.00$, $J = 0.67$). The outflow angle of Model V1 changes dramatically for the reason that it has the lowest value of consistence as well as the ability of recovering swirl, while Model V3 is characterized by the most uniform value which shows no more than 4° difference along the spanwise direction under individual conditions. It is reasonable to say that the swirl behind the propeller is well controlled or recovered to varying degrees with each SRV, and obviously Model V3 is most prominent in this work with the most potential for full use of the swirl. Thus Model V3 is chosen as the base case in the following study.

4.3. Aerodynamic performance analysis

4.3.1. Impact on propeller

The addition of thrust at the design point consists of two parts: the thrust of the propeller has increased from 44.78 N for an isolated rotor to 46.88 N for a rotor with Model V3, contributing 4.69% extra thrust, while the vane provides additional 0.48 N thrust, representing 1.07% extra thrust. This improvement may lead to a desirable effect that a propeller with SRVs tends to have a lower rotating speed when the same amount of thrust is obtained which can be appropriate for a decrease in noise.

However, the upstream propeller has uploaded due to the interference with the downstream vane. The torque has increased from 3.596 N·m for an isolated rotor to 3.903 N·m for a rotor with Model V3, with increment accounting for 8.54%, which counteracts that of thrust. Therefore, there is a decrease in efficiency after mounting the SRVs at this point. As shown above, the main contributor of thrust goes to the rotor, which leaves the vane to be better modified to provide more thrust and make use of the energy of swirl sufficiently.

4.3.2. Aerodynamic performance of SRVs

Just like Fig. 7, Fig. 12 depicts the axial distributions of the axial velocity V_z at $r/R = 0.57$ in the presence of SRVs. The

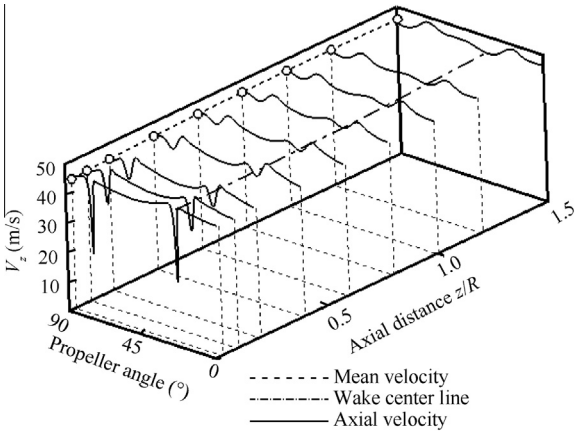

Fig. 12 Axial distribution of V_z behind SRVs, $r/R = 0.57$ and $J = 1.00$.

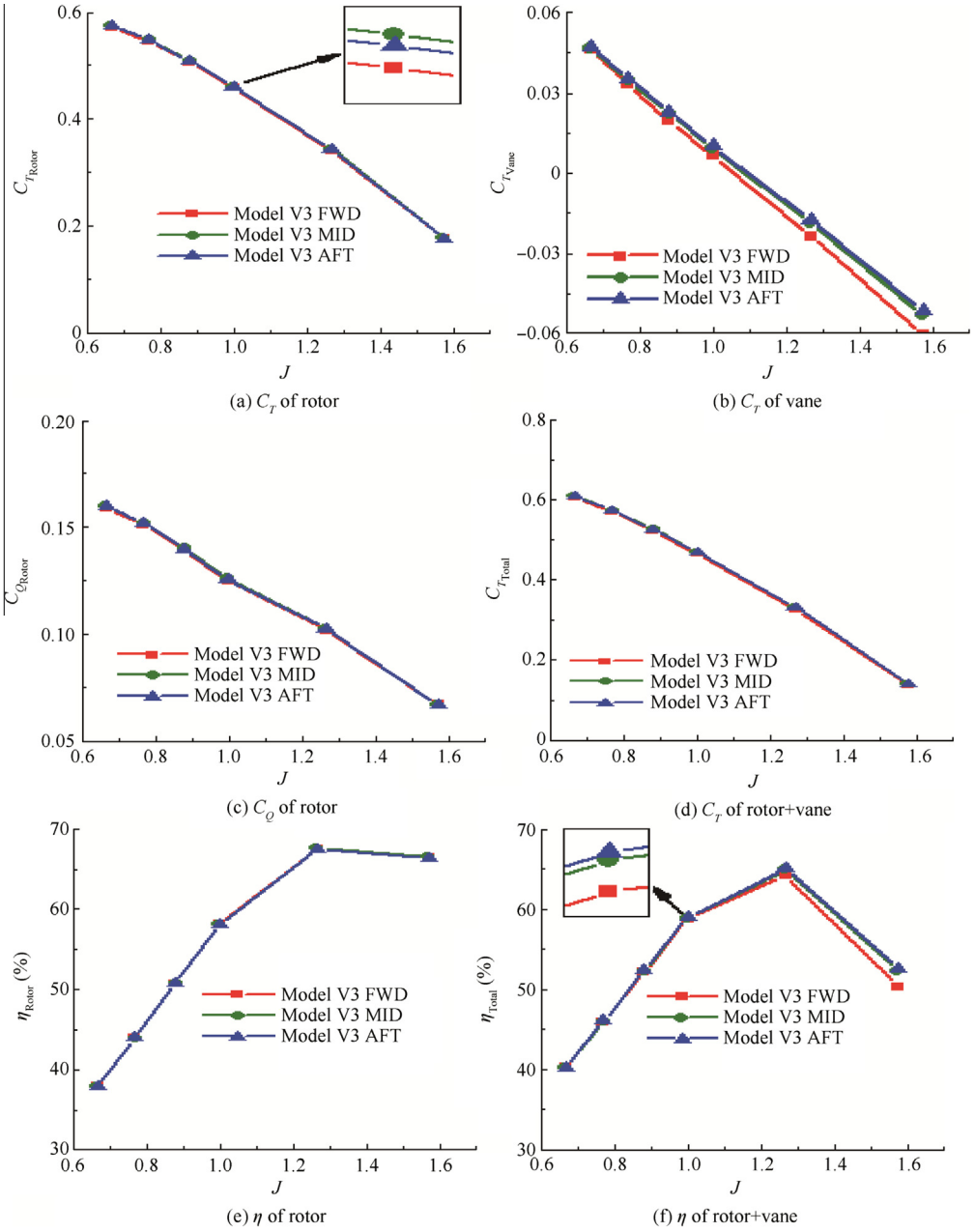

Fig. 13 Total performance of the propeller with Model V3 of different axial distances.

stacking line of SRVs is located at the corresponding position of $z/R = 0.38$ in Fig. 7(a), and the initial plane corresponds to $z/R = 0.51$. The center of blade wake (the dash dot line) is almost parallel to the axis, which is indicative of a successful elimination of the swirl behind the propeller as expected. The vane thrust also comes from the swirl recovery: the axial momentum of fluid rises after passing through the vanes, causing an equal and opposite force on SRVs which depends on the magnitude and angle of the inflow.

5. Vane position study

The axial distance of the stacking point of rotor and vane was set to $z/c_0 = 2.0$ (base case), 2.5, and 3.0 separately (denoted as V3 forward (FWD), V3 middle (MID), and V3 after (AFT)) to study the influence of SRV axial positions. As shown in Fig. 13, the propeller thrust experiences less increment with V3 FWD, possibly for the reason that the slipstream zone of the propeller is contractive, so SRVs have a smaller effective blockage area with a forward position. It can be inferred that there is an optimum axial position range for SRVs to provide the propeller with the most thrust increment, which is not too adjacent to the propeller with a weaker block effect due to the contractive slipstream, and not too far from the propeller with smaller blades interaction resulting from a far axial distance. SRVs at the middle and afterward positions are just in the optimum range for the fact that their performance curves are almost overlapped. The same results can also be concluded from Fig. 13(b).

n conclusion, the axial position of SRVs has limited effect on the performance of the propeller, but in a certain degree, the propeller shows better performance with mid and aft vanes.

6. Conclusions

(1) The numerical strategy was validated from two aspects of global quantities as well as the local flow field of an isolated propeller to determine the numerical methods for further study. The velocity profile of the slipstream zone and the wake development of the propeller were discussed to provide design conditions for SRVs.
(2) Three types of SRVs with different consistence profiles were designed and the following conclusions can be made: the propeller has an increased load capability with SRVs behind it, showing both larger thrust and torque coefficients; the swirl behind the propeller is successfully recovered with all three vanes, and Model V3 which is of the most divergent shape has the most uniform outflow angle at multiple operating conditions; the total thrust has increased 5.76% at the design point ($J = 1.00$) for a propeller with Model V3, but a lower efficiency results from even larger absorbed power; the main contributor of thrust goes to the rotor which is indicative of the requirement of further work for a better vane design and the choice of a vane working point for the improvement of total efficiency.
(3) The axial distance between rotors and vanes has little influence upon the total performance at low advance ratios no more than 1.00, but shows considerable effects at higher values within the difference of 2.3% in total efficiency. There is an optimum axial position range for SRVs corresponding to the highest efficiency and thrust coefficient.

Acknowledgement

The technical assistance from the TU Delft in providing the experimental data is of great appreciation. This work was supported by the National Natural Science Foundation of China (No. 51376150). All these supports are gratefully acknowledged.

References

1. Holmes BJ, Durham MH, Tarry SE. Small aircraft transportation system concept and technologies. *J Aircraft* 2004;**41**(1):26–35.
2. van Blyerburgh P. UAVs: an overview. *Air Space Eur* 1999;**1**(5):43–7.
3. Alexander D, Guynn M, Lee Y-M, Bushnell D. Emissionless aircraft study. *Proceedings of the 38th AIAA/ASME/SAE/ASEE joint propulsion conference & exhibit*; 2002 Jul 7–10; Indianapolis, Indiana, USA; 2002.
4. Mitchell GA, Mikkelson DC. Summary and recent results from the NASA advanced high-speed propeller research program. *Proceedings of the 18th joint propulsion conference*; 1982 Jun 21–23; Cleveland OH, USA; 1982.
5. Jeracki RJ, Mikkelson DC, Blaha BJ. Wind tunnel performance of four energy efficient propellers designed for Mach 0.8 cruise. *Proceedings of business aircraft meeting*; 1979 Apr 3–6; Wichita Kansas, USA; 1979.
6. Rohrbach C. A report on the aerodynamic design and wind tunnel test of a prop-fan model. *Proceedings of the 12th propulsion conference*; 1976 Jul 26–29; Palo Alto, USA; 1976.
7. Mikkelson DC, Blaha BJ, Mitchell GA, Wikete JE. Design and performance of energy efficient propellers for Mach 0.8 cruise. *Proceedings of business aircraft meeting and exposition*; 1977 Mar 29–April 1; Wichita Kansas, USA; 1979.
8. Li J, Gao ZH, Huang JT, Zhao K. Aerodynamic design optimization of nacelle/pylon position on an aircraft. *Chin J Aeronaut* 2013;**26**(4):850–7.
9. Dittmar JH, Blaha BJ, Jeracki RJ. Tone noise of three supersonic helical tip speed propellers in a wind tunnel. *Proceedings of the 97th meeting of the acoustical society of AM*; 1979 Jun 11–15; Cambridge Massachusetts, USA; 1979.
10. Revell JD, Balena FJ, Koval LR. Analytical study of interior noise control by fuselage design techniques on high-speed, propeller-driven aircraft. Final report. Burbank: Lockheed-California Co.; 1979 Jul-1979 Dec. Report No.: NASA-CR-159222, LR-29382, LR-29252. Contract No.: NAS1-15427.
11. Biermann D, Gray WH. Wind-tunnel tests of eight-blade single- and dual-rotating propellers in the traction position. Hampton (VA): National Aeronautics and Space Admin, Langley Research Center; 1941. Report No.: NACA-WR-L-384.
12. Wainauski HS, Vaczy CM. Aerodynamic performance of a counter rotating Prop-Fan. *Proceedings of the 22nd AIAA/ASME/SAE/ASEE joint propulsion conference*; 1986 Jun 16–18; Huntsville AL, USA; 1986.
13. Strack WC, Knip G, Weisbrich AL. Technology and benefits of aircraft counter rotation propellers. Cleveland (OH): National Aeronautics and Space Administration, Lewis Research Center; 1981. Report No.: N-8311129; NASA-TM-82983; E-1414.
14. Gazzaniga JA, Rose GE. Wind tunnel performance results of swirl recovery vanes as tested with an advanced high speed propeller. *Proceedings of the 28th AIAA/ASME/SAE/ASEE joint propulsion conference and exhibit*; 1992 Jul 6–8; Nashville TN, USA; 1992.
15. Dittmar JH, Hall DG. The effect of swirl recovery vanes on the cruise noise of an advanced propeller. *Proceedings of the AIAA 13th aeroacoustics conference*; 1990 Oct 22–24; Tallahassee FL, USA; 1990.
16. van Berkel ECR, Kotsonis M, Veldhuis LLM, Eitelberg G. Influence of non-uniform inflow conditions on propeller performance in tractor configuration. Experimental research report; 2012 Nov.
17. Lavich PL, McCormick DC, Parzych DJ. Vortex structure of wakes behind an advanced propeller at takeoff load conditions. *Proceedings of the AIAA space programs and technologies conference*; 1990 Oct 22–24; Tallahassee FL, USA; 1990.

Wang Yangang is a professor and Ph.D. advisor in the School of Power and Energy at Northwestern Polytechnical University in Xi'an, China, where he received his Ph.D. degree in 2004. His current research interests are computational fluid dynamic for turbomachinery, flow control, and blade design technique.

Li Qingxi is a master student majoring in aerospace propulsion theory and engineering in the School of Power and Energy at Northwestern Polytechnical University in Xi'an, China.

G. Eitelberg is a full professor in Delft University of Technology whose major interests are flight performance and propulsion. He is also the managing director of the German-Dutch Wind Tunnels.

L.L.M. Veldhuis is a full professor in Delft University of Technology whose major interests are propeller propulsion and its integration.

M. Kotsonis is an assistant professor in Delft University of Technology who is devoted to using plasma to make the aircraft more efficient.